



Evidence for tropospheric wind shear excitation of high-phase-speed gravity waves reaching the mesosphere using the ray-tracing technique

M. Pramitha¹, M. Venkat Ratnam¹, A. Taori¹, B. V. Krishna Murthy², D. Pallamraju³, and S. Vijaya Bhaskar Rao⁴

¹National Atmospheric Research Laboratory (NARL), Gadanki, India

²B1, CEBROS, Chennai, India

³Physical Research Laboratory (PRL), Ahmadabad, India

⁴Department of Physics, Sri Venkateswara University, Tirupati, India

Correspondence to: M. Venkat Ratnam (vratnam@narl.gov.in)

Received: 20 May 2014 – Published in Atmos. Chem. Phys. Discuss.: 29 July 2014

Revised: 12 February 2015 – Accepted: 14 February 2015 – Published: 10 March 2015

Abstract. Sources and propagation characteristics of high-frequency gravity waves observed in the mesosphere using airglow emissions from Gadanki (13.5° N, 79.2° E) and Hyderabad (17.5° N, 78.5° E) are investigated using reverse ray tracing. Wave amplitudes are also traced back, including both radiative and diffusive damping. The ray tracing is performed using background temperature and wind data obtained from the MSISE-90 and HWM-07 models, respectively. For the Gadanki region, the suitability of these models is tested. Further, a climatological model of the background atmosphere for the Gadanki region has been developed using nearly 30 years of observations available from a variety of ground-based (MST radar, radiosondes, MF radar) and rocket- and satellite-borne measurements. ERA-Interim products are utilized for constructing background parameters corresponding to the meteorological conditions of the observations. With the reverse ray-tracing method, the source locations for nine wave events could be identified to be in the upper troposphere, whereas for five other events the waves terminated in the mesosphere itself. Uncertainty in locating the terminal points of wave events in the horizontal direction is estimated to be within 50–100 km and 150–300 km for Gadanki and Hyderabad wave events, respectively. This uncertainty arises mainly due to non-consideration of the day-to-day variability in the tidal amplitudes. Prevailing conditions at the terminal points for each of the 14 events are provided. As no convection in and around the terminal points is noticed, convection is unlikely to be the source. Interestingly, large ($\sim 9 \text{ m s}^{-1}$

km^{-1}) vertical shears in the horizontal wind are noticed near the ray terminal points (at 10–12 km altitude) and are thus identified to be the source for generating the observed high-phase-speed, high-frequency gravity waves.

1 Introduction

Atmospheric gravity waves (GWs) play an important role in the middle atmospheric structure and dynamics. They transport energy and momentum from the source region (mainly troposphere) to the upper atmosphere. The waves are dissipated upon reaching a critical level, transferring energy and momentum to the mean flow and leading to changes in the thermal structure of the atmosphere (Fritts and Alexander 2003). Several sources are identified for the generation of GWs, which include deep convection, orographic effect, vertical shear of horizontal wind and geostrophic adjustment. For GW generation from deep convection, mainly three mechanisms are considered (Fritts and Alexander 2003). These are (i) pure thermal forcing (e.g., Salby and Garcia 1987; Alexander et al., 1995; Piani et al., 2000; Fritts and Alexander 2003; Fritts et al., 2006), (ii) the mechanical oscillator effect (e.g., Clark et al., 1986; Fovell et al., 1992) and (iii) the obstacle effect (e.g., Clark et al., 1986; Pfister et al., 1993; Vincent and Alexander 2000). The importance of these depends upon the vertical profile of local shear and time dependence of latent heat release. GWs from the convec-

tion source can have a wide range of phase speeds, frequencies and wavelengths, unlike those from orography, which are generally confined to low ground-based frequencies and phase speeds (e.g., Queney, 1948; Lilly and Kennedy 1973; Nastrom and Fritts 1992; Eckermann and Preusse 1999; Alexander et al., 2010). In the shear excitation mechanism, mainly two processes, namely sub-harmonic interaction and envelope radiation (Fritts and Alexander 2003), are considered. The latter process can yield horizontal scales of a few tens of kilometers and phase speeds comparable to the mean wind. The geostrophic adjustment source is effective mainly in high latitudes (e.g., O'Sullivan and Dunkerton 1995; Shin Suzuki et al., 2013; Plugonven and Zhang 2014).

In general, significant progress has been made in the understanding of the physical processes leading to the spectrum of GWs through both observations and modeling. However, identification of the exact sources for the generation of GWs and their parameterization in the models remains a challenge (Geller et al., 2013). In order to identify the gravity wave sources, hodograph analysis has been widely used. Hodograph analysis can be used to identify the gravity wave parameters, which can be used as input parameters to the ray tracing. With the hodograph, the direction of propagation of the wave and hence the location of the source can be ascertained. However, this method is applicable only for medium- and low-frequency waves, as for the high-frequency GWs the hodograph will not be an ellipse but nearly a straight line. Further, as it assumes monochromatic waves, it is not always applicable in the real atmosphere. Notwithstanding this limitation, with this method, convection and vertical shear have been identified as the possible sources of the observed medium and low-frequency GWs in the troposphere and lower stratosphere over many places (e.g., Venkat Ratnam et al., 2008). It becomes difficult to apply this method for GWs that are observed in the mesosphere and lower thermosphere (MLT) region, where simultaneous measurements of temperatures (with wind) would not be available.

A more appropriate method in such cases is ray tracing (Marks and Eckermann 1995), which is widely used to identify the sources of GWs observed at mesospheric altitudes. Several studies (Hecht et al., 1994; Taylor et al., 1997; Nakamura et al., 2003; Gerrard et al., 2004; Brown et al., 2004; Wrasse et al., 2006; Vadas et al., 2009; and references therein) have been carried out to identify the sources for the GWs observed in the mesosphere using airglow images and in the stratosphere using radiosonde and lidar data (Guest et al., 2000; Hertzog et al., 2001). In mesospheric studies, important GW parameters, such as periodicities and horizontal wavelengths (and sometimes vertical wavelengths when two imagers are simultaneously used), are directly derived. A major limitation to the ray-tracing method is the non-availability of realistic information on the background atmosphere. This is difficult to obtain with the available suite of instrumentation for rendering identification of the source of the waves. Nevertheless, possible errors involved in identifying the ter-

minal point of the waves with and without realistic background atmosphere have been estimated (e.g., Wrasse et al., 2006; Vadas et al., 2009).

Over the Indian region, several studies (Venkat Ratnam et al., 2008, and references therein) have been carried out for extracting GW parameters using various instruments (MST radar, radiosondes, lidar and satellite observations). In a few studies (Kumar, 2006, 2007; Dhaka et al., 2002; Venkat Ratnam et al., 2008; Debashis Nath et al., 2009; Dutta et al., 2009; Leena et al., 2012a, b), possible sources in the troposphere for their generation are identified which include convection, wind shear and topography.

In the present investigation, a reverse ray-tracing method is implemented to identify the sources of the GWs at mesospheric altitudes observed from an airglow imager located at Gadanki (13.5° N, 79.2° E) and from a balloon experiment which carried an ultraviolet imaging spectrograph from Hyderabad (17.5° N, 78.5° E). Wave amplitudes are also traced back, including both radiative and diffusive damping. In Sect. 2 we described the instrumentation, in Sect. 3 the theory behind ray tracing, in Sect. 4 the background atmosphere used for ray tracing, in Sect. 5 application of the ray-tracing method and in Sect. 6 identification of the sources of the observed waves.

2 Database

2.1 Airglow imager observations at Gadanki and methodology for extracting GW characteristics

The NARL Airglow Imager (NAI) located at Gadanki is equipped with a 24 mm Mamiya fisheye lens. It can monitor OH, O(¹S) and O(¹D) emissions and has a 1024 × 1024 pixel CCD as the detector, and has a field of view of 90°, avoiding nonlinearity arising at higher zenith angles. In the present study, only observations of O(¹S) emission which originate at ~93–100 km (with a peak emission altitude of ~97 km) are used. The exposure time used to measure the intensities of emissions was 70 s. After the image was captured, it was analyzed and corrected for the background brightness, star brightness and actual coordinates. The area covered in the image is 200 km × 200 km with a spatial resolution of 0.76 km near zenith and 0.79 km at the edges. More details on the NAI are discussed by Taori et al. (2013).

We observed three wave events between 14:29 and 14:51, 15:44 and 15:50, and 20:45 and 21:17 UTC, respectively, on 17 March 2012 (Fig. 1), as well as two wave events between 15:47 and 16:27 and between 16:31 and 16:54 UTC, respectively, on 19 March 2012 in the O(¹S) airglow emission intensities. In these images, crests of the waves are emphasized by yellow freehand lines, and the motion of the waves is apparent in the successive images shown one below the other. Red arrows indicate the direction of the propagation of the waves. Horizontal wavelengths of the GWs are determined

Table 1. GW characteristics (direction of propagation, ϕ ; horizontal wavelength, λ_h ; vertical wavelength, λ_z ; period, T ; phase speed, C ; and intrinsic frequency, ω_{ir}) for events observed over Gadanki (G) and Hyderabad (H). The terminal point locations (latitude, longitude and altitude) are also shown for each event. Conditions leading to the termination for each wave event are also shown. Events for which ray paths terminated at mesospheric altitude are indicated with an asterisk.

Events	ϕ (degrees)	λ_h (km)	T (min)	C (m s ⁻¹)	Longitude (degrees)	Latitude (degrees)	Altitude (km)	ω_{ir} (rad s ⁻¹)	Termination condition
Gadanki location									
G1	102	85(26)	18	78	79.9	10.8	13	0.00058	$m^2 < 0$
G2	98	34(28.9)	9	63	79.4	12.3	17	0.0116	WKB > 1
G3	132	12(13.6)	6	33	79.2	13.37	96.9*	0.0006	Intrinsic frequency approaching zero
G4	62	134(40)	12	186	79.14	13.2	92.9*	0.0093	WKB > 1
G5	142	16(2)	8	33	79.9	12.7	66.9*	0.0156	WKB > 1 and $m^2 < 0$
Hyderabad location									
H1	11	39(23.7)	16	41	70.2	15.8	10.5	0.0028	WKB > 1
H2	16	57(31.5)	16	59	75.3	16.4	13.5	0.0046	WKB > 1
H3	21	74(39)	16	77	75.9	16.3	14.5	0.0049	WKB > 1
H4	11	39(19.6)	20	32.5	76.3	17.1	67.6*	0.00083	$m^2 < \text{limiting condition}$ and intrinsic frequency approaching zero
H5	16	57(25)	20	48	72.7	15.7	12.5	0.0029	WKB > 1
H6	21	74(31)	20	61.7	74.7	15.8	13.5	0.0035	WKB > 1
H7	11	39(17.7)	23	28	75.8	16.9	68.5*	0.00087	$m^2 < \text{limiting condition}$ and intrinsic frequency approaching zero
H8	16	57(23)	23	41	68.3	14.8	11.5	0.0022	WKB > 1
H9	21	74(27)	23	54	73.4	15.4	13.5	0.0032	WKB > 1

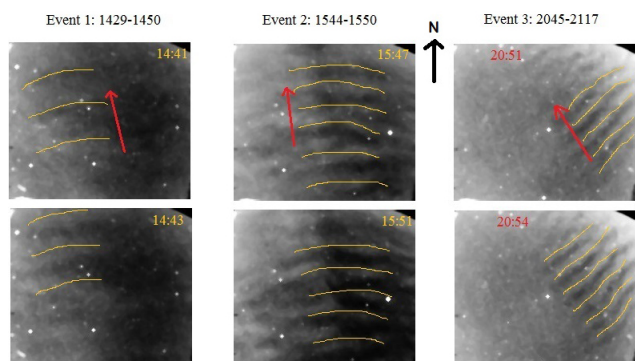


Figure 1. Identification of three wave events (left to right) obtained from the airglow emission intensities originating from O(¹S) emissions from Gadanki. The wave crests are emphasized by yellow freehand lines. Motion of waves can be obtained by successive images and the direction of propagation is shown by red arrows. Time of occurrence of events is shown in each image in UT (hh:mm).

by applying 2-D FFT (fast Fourier transform) to the observed airglow images. The periods of the GWs are estimated by applying 1-D FFT in time to the complex 2-D FFT in space. Direction of propagation and phase speed of GWs are identified using successive images. More details of the method-

ology for estimating the GW parameters from NAI observations are provided in Taori et al. (2013). Table 1 summarizes the GW parameters extracted from the five wave events (G1 to G5) mentioned above. In general, the waves corresponding to these events are moving in the NNW direction. Zonal (k) and meridional (l) wave numbers are calculated using the relations $k = k_h \cos \phi$ and $l = k_h \sin \phi$, where k_h is the horizontal wave number and ϕ is the horizontal direction of propagation observed from the airglow imager. The vertical wavelengths are calculated using the GW dispersion relation

$$\omega_{ir}^2 = \frac{N^2(k^2 + l^2) + f^2(m^2 + \alpha^2)}{k^2 + l^2 + m^2 + \alpha^2}, \quad (1)$$

where ω_{ir} is the intrinsic frequency of the wave, N is the Brunt–Väisälä frequency, f is the Coriolis frequency and m is the vertical wave number. Zonal, meridional and vertical wavelengths can be derived from the parameters given in Table 1. The background atmosphere used for ray tracing is developed using 30 years of observations from various sources and will be discussed more in Sect. 4.

2.2 Daytime GW observations at Hyderabad obtained through optical emissions

A multi-wavelength imaging echelle spectrograph (MISE) is used to obtain daytime emission intensities of oxygen emissions at 557.7, 630.0 and 777.4 nm in the MLT region at Hyderabad. MISE obtains high-resolution spectra of daytime skies which are compared with the reference solar spectrum. The difference obtained between the two yields information on the airglow emissions. The details of the emission extraction process and calibration procedures of the emission intensities and the salient results obtained in terms of wave coupling of atmospheric regions demonstrating the capability of this technique have been described elsewhere (Pallamraju et al., 2013; Laskar et al., 2013). In the present experiment, the slit oriented along the magnetic meridian enabled information on the meridional scale size of waves (λ_y) at O(¹S) emission altitude of ~ 100 km (in the daytime). An ultraviolet imaging spectrograph with its slit oriented in the east–west direction was flown on a high-altitude balloon (on 8 March 2010), which provided information on the zonal scale sizes of waves (λ_x) using the OI 297.2 nm emissions that originate at ~ 120 km. Both MISE and UVIS are slit spectrographs with array detectors providing 2-D information, with one direction yielding high-spectral-resolution spectrum (0.012 nm at 589.3 nm and 0.2 nm at 297.2 nm for MISE and UVIS, respectively) and the orthogonal direction yielding information on the dynamics over 330 km (in the y direction for OI 557.7 nm emission) and 170 km (in the x directions for the OI 297.2 nm emission). The spatial resolutions of these measurements are around 50 and 11 km, respectively. The details of the experiment and the wave characteristics in terms of λ_x , λ_y , λ_H (horizontal scale sizes), time periods (τ), propagation speeds (c_H) and propagation direction (θ_H) obtained by this instrument at a representative altitude of 100 km are described in detail in Pallamraju et al. (2014). Nine events from this experiment which occurred on 8 March 2010 are considered in the present study for investigating their source regions and are marked as H1 to H9 in Table 1. All wave events observed at Gadanki and Hyderabad correspond to high-frequency, high-phase-speed gravity waves as seen from their large vertical wavelengths, small periods and high phase speeds (Table 1).

2.3 Outgoing long-wave radiation (OLR) and brightness temperature in the infrared band (IR BT)

Satellite data of OLR/IR BT are used as a proxy for tropical deep convection. In general, the daily NOAA interpolated OLR can be used to obtain information on the synoptic-scale convection. However, for local convection on smaller spatial and temporal scales, the IR BT data merged from all available geostationary satellites (GOES-8/10, METEOSAT-7/5 GMS) are obtained from the National

Center for Environment Prediction (NCEP) Climate Prediction Center (source: <ftp://disc2.nascom.nasa.gov/data/s4pa/TRMM Ancillary/MERG/>). The merged IR BT with a pixel resolution of 4 km is available for 60° N to 60° S (geostationary). The data in the east–west direction begin from 0.082° E with a grid increment of 0.03637° longitude and those in the north–south direction from 59.982° N with a grid increment of 0.03638° latitude (Janowiak et al., 2001). The BT data set is retrieved for every half-hour interval over regions of $\pm 5^\circ$ around Gadanki and Hyderabad on 17 March 2012 and 8 March 2010, respectively, to see whether any convective sources were present in these locations. Since the waves under study are high-frequency waves propagating at high phase speeds with smaller horizontal wavelengths, a maximum $5^\circ \times 5^\circ$ grid is considered to be adequate. In general, the regions with $OLR < 240 \text{ W/m}^2$ are treated as convective areas.

3 Reverse ray-tracing method

We followed the treatment of ray tracing given by Marks and Eckermann (1995). Note that the ray-tracing theory is applicable only when WKB (Wentzel–Kramers–Brillouin) approximation is valid. When the WKB parameter δ given by

$$\delta = \frac{1}{m^2} \left| \frac{\partial m}{\partial z} \right| \approx \left| \frac{1}{C_{gz} m^2} \frac{dm}{dt} \right| \quad (2)$$

(where C_{gz} is the vertical group velocity, m is the vertical wave number, t is the time and z is the altitude) is less than unity, the approximation is taken to be valid.

In order to calculate the wave amplitude, we used the wave action equation of the form

$$\frac{\partial A}{\partial t} + \nabla \cdot (C_g A) = -\frac{2A}{\tau}, \quad (3)$$

where $A = E/\omega_{ir}$ represents the wave action density; C_g represents the group velocity vector; and $E = \frac{\rho_0}{2} [u'^2 + v'^2 + w'^2 + N^2 \zeta'^2]$ represents the wave energy density, which is the sum of kinetic and potential energy components, as described by wave perturbations in zonal, meridional and vertical velocities (u' , v' , w'), as well as vertical displacement (ζ'). Here ρ_0 is the background density and τ is the damping timescale (Marks and Eckermann, 1995). Using the peak horizontal velocity amplitude along the horizontal wave vector we can calculate the wave action density using the equation

$$A = \frac{1}{4} \frac{\rho_0 |\hat{u}|^2}{\omega_{ir}} \left\{ 1 + \frac{f^2}{\omega_{ir}^2} + \frac{N^2 + \omega_{ir}^2}{N^2 - \omega_{ir}^2} \left(1 - \frac{f^2}{\omega_{ir}^2} \right) \right\}. \quad (4)$$

In order to avoid spatial integration in the wave action equation we can write Eq. (3) in terms of the vertical flux of wave action $F = C_{gz} A$, where F is the vertical flux of wave action

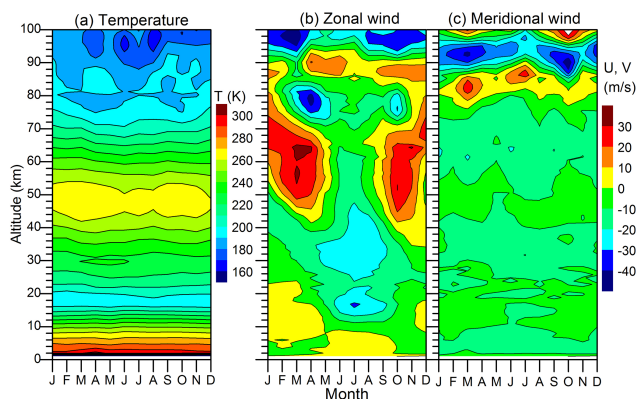


Figure 2. Climatological monthly mean contours of (a) temperature, (b) zonal wind and (c) meridional wind obtained over Gadanki region combining a variety of instruments listed in Table 2.

and C_{gz} is vertical component of the group velocity. Assuming negligible contribution from higher-order terms, Eq. (4) can be written as

$$\frac{dF}{dt} = -\frac{2}{\tau}F. \quad (5)$$

As the wave moves through the atmosphere, amplitude damping takes place, which is mainly due to eddy diffusion and infrared radiative cooling by CO_2 and O_3 . At higher altitudes (above about 100 km), molecular diffusion becomes important as compared to the eddy diffusion. We can calculate the damping rate due to diffusion using

$$\tau_D^{-1} = D(k^2 + l^2 + m^2 + \alpha^2), \quad (6)$$

where $D = D_{\text{Eddy}} + D_{\text{molecular}}$ represents the sum of eddy and molecular diffusivities. Details of the calculation of D are given in the next section. In order to calculate the infrared radiative damping from 20 to 100 km, we used the damping rate calculation method given by Zhu (1993). The total damping rate is calculated using the following equation:

$$\tau^{-1} = \frac{\tau_r^{-1} \left(\frac{1-f^2/\omega_{\text{ir}}^2}{1-\omega_{\text{ir}}^2/N^2} \right) + \tau_D^{-1} \left(1 + \frac{f^2}{\omega_{\text{ir}}^2} + \frac{1-f^2/\omega_{\text{ir}}^2}{N^2/\omega_{\text{ir}}^2-1} + Pr^{-1} \frac{1-f^2/\omega_{\text{ir}}^2}{1-\omega_{\text{ir}}^2/N^2} \right)}{\left\{ 1 + \frac{f^2}{\omega_{\text{ir}}^2} + \frac{N^2+\omega_{\text{ir}}^2}{N^2-\omega_{\text{ir}}^2} \left(1 - \frac{f^2}{\omega_{\text{ir}}^2} \right) \right\}}, \quad (7)$$

where Pr is Prandtl number. Note that the damping effect will be less for high-frequency wave.

4 Background atmosphere

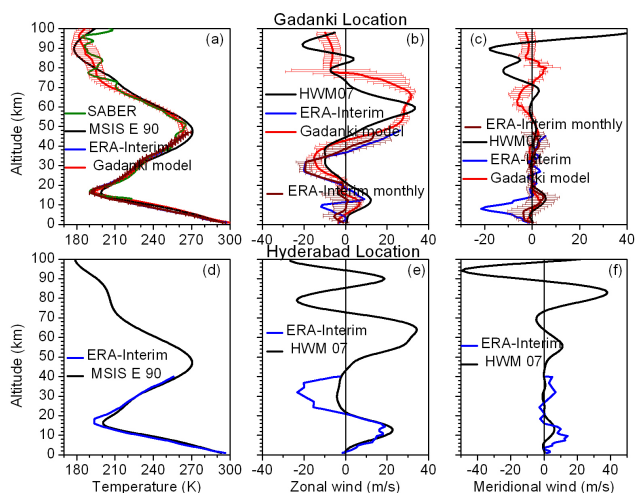
In order to carry out reverse ray tracing, information on background atmospheric parameters (U , V and T) is required

right from the initial point (mesosphere) to the termination point (frequently in the troposphere). In general, there is no single instrument which can probe the troposphere, stratosphere and mesosphere simultaneously. Note that in order to trace the ray we require atmospheric parameters for a specified latitude–longitude grid. Since the observed wave events belong to high frequencies (GWs with short horizontal wavelengths and high vertical wavelengths), we require the background information for grid sizes of at least $5^\circ \times 5^\circ$ around Gadanki and Hyderabad. For the information on temperature and density at the required grids, we used Extended Mass Spectrometer and Incoherent Scatter Empirical (MSISE-90) model data (Hedin, 1991) from the surface to 100 km with an altitude resolution of 0.1 km for a $0.1^\circ \times 0.1^\circ$ grid around these locations. Note that the MSISE-90 model is an empirical model which provides temperature and density data from the surface to the thermosphere. For horizontal winds at the required grids, we used the outputs from the Horizontal Wind Model (HWM-07) (Drob et al., 2008) data. This model was developed by using a total of 60×10^6 observations available from 35 different instruments spanning 50 years. Further, long-term data available from a variety of instruments (MST radar, MF radar, rocketsondes, radiosondes, HRDI/UARS and SABER/TIMED satellites) in and around ($\pm 5^\circ$) Gadanki have been used to develop a background climatological model profiles of U , V and T on a monthly basis. Details of the data used to develop the background temperature, and horizontal winds are provided in Table 2. Monthly mean contours of temperature, zonal and meridional winds obtained from the climatological model (from now on referred to as the Gadanki model) are shown in Fig. 2. In general, significant features of the background atmospheric structure for a typical tropical region can be noticed from this figure. Tropopause, stratopause and mesopause altitudes are located at around 16–18, 48–52 and 98–100 km with temperatures of 190–200, 260–270 and 160–170 K, respectively. Mesospheric semiannual oscillation around 80–85 km is also seen (Fig. 2a). The Tropical Easterly Jet at around 16 km during the Indian summer monsoon season (June–July–August) and semiannual oscillation near the stratopause (and at 80 km with different phase) are also clearly visible in the zonal wind (Fig. 2b). Meridional winds do not exhibit any significant seasonal variation in the troposphere and stratosphere but show large variability in the mesosphere (Fig. 2c). These overall features in the background temperature and wind match well with those reported considering data from different instruments by Kishore Kumar et al. (2008a, b).

The profiles of T obtained from the MSISE-90 model and U and V from HWM-07 for 17 March 2012 are shown in Fig. 3a and 3b and c, respectively. The Gadanki model mean temperature profile for the month of March and the temperature profile obtained from TIMED/SABER and mean temperature obtained from ERA-Interim for the month of March 2012 are also superimposed in Fig. 3a for comparison. Very

Table 2. Details of instruments and parameters measured, altitude range in which data are available, and the duration of the data considered for developing the Gadanki atmospheric model.

Instrument (parameter(s) obtained)	Altitude range covered	Duration of the data considered
Indian MST radar (U , V)	4–21 and 65–85 km	1996–2012
Radiosonde (U , V , T)	1–30 km	2006–2012
Lidar (T)	30–75 km	1998–2012
Rocket (U , V , T)	22–80 km	1970–1991, 2002–2007
HALOE, HRDI/UARS (T , U , V)	65–110 km	1991–2000
SABER/TIMED (T)	30–110 km	2002–2012

**Figure 3.** Profiles of (a) temperature (b) zonal wind and (c) meridional wind obtained using ERA-Interim data products for 17 March 2012, 12:00 UTC, over the Gadanki region. Profiles obtained from a variety of sources over Gadanki (Gadanki model) listed in Table 2 are also superimposed in the respective panels for comparison. Plots (d–e) are same as (a–c) but obtained for Hyderabad on 8 March 2010. The temperature profile obtained from MSISE-90 and the zonal and meridional winds obtained from HWM-07 for the same day are also provided in the respective panels.

good agreement between the profiles can be noticed. The profiles of U and V obtained from the Gadanki model for the month of March and also the monthly mean of the ERA-Interim are also superimposed in Fig. 3b and c, respectively. In general, a good match is seen between the Gadanki model and ERA-Interim and HWM-07 models up to the altitude of the stratopause. The differences between the two above the stratopause could be due to tidal winds, which have large amplitudes at mesospheric altitudes. Though tidal amplitudes are already included in the HWM-07 model, their day-to-day variability may be contributing to these differences. In order to avoid any bias due to day-to-day variability of the tides at mesospheric altitudes, we have considered tidal amplitudes of 5, 10 and 15 K in temperature and 10, 20 and 30 m s^{-1} in wind at 97 km to represent day-to-day variability.

In general, the troposphere is a highly dynamic region, though the amplitudes of tides are considerably small. In order to consider more realistic horizontal winds in the troposphere and stratosphere, we further considered the ERA-Interim products (Dee et al., 2011). These data are available at 6 h intervals with a $1.5^\circ \times 1.5^\circ$ grid resolution at 37 pressure levels covering from the surface (1000 hPa) to the stratopause (~ 1 hPa). The profiles of T , U and V from ERA-Interim for 17 March 2012 for 12:00 UTC are also superimposed in Fig. 3a, b and c, respectively. In general, good agreement between the other models and ERA-Interim model can be noticed, particularly in V in the lower and upper levels, except between 10 and 20 km. To summarize, we have considered the following wind models: (1) ERA-Interim (from the surface to 40 km) and HWM-07 models from 40 to 100 km, (2) the Gadanki model and (3) zero wind ($U = 0$ and $V = 0$). Using these background atmosphere profiles, we calculated the relevant atmospheric parameters like N^2 and H . Profiles of T , U and V obtained using ERA-Interim data products for 8 March 2010, 06:00 UTC, over the Hyderabad region are shown in Fig. 3d–f, respectively. T , U and V profiles as obtained from MSISE-90 and HWM-07 for the same day are also provided in the respective panels. The background atmosphere information for wave events over Hyderabad is obtained in a manner similar to that mentioned above for Gadanki.

In order to calculate diffusive damping, we used eddy diffusivity profiles for the troposphere and lower stratosphere and mesosphere which are obtained using MST radar (Narayana Rao et al., 2001) at Gadanki as shown in Fig. 4a. In the altitude regions where there are data gaps, we extrapolated/interpolated the diffusivity profiles, and the approximated profile with different analytical exponential functions are also shown in Fig. 4a. The eddy diffusivity profile of Hocking (Hocking, 1991) that is presented in Marks and Eckermann (1995) is also superimposed for comparison. Note that Hocking's profile corresponds mainly to midlatitudes. In general, eddy diffusivity is relatively higher in Hocking's profile than in the Gadanki profile. This same (Gadanki) profile is also used for Hyderabad events. In Fig. 4b, molecular diffusivity is shown. It is seen that the molecular diffusivity exceeds the eddy diffusivity at altitudes > 80 km.

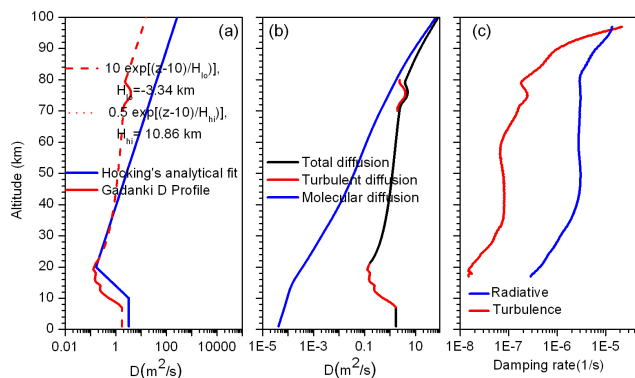


Figure 4. (a) Profile of eddy diffusivity (thick red line) obtained from Gadanki MST radar (Rao et al., 2001) in the troposphere, lower stratosphere and mesosphere. A fitted profile (dotted line) with exponential function is also shown. Hocking's (Hocking 1991) analytical curve (extrapolated) is also superimposed for comparison. (b) Profiles of eddy, molecular and total diffusivity. (c) Radiative and diffusive damping rates.

We have also taken into account molecular diffusivity in the ray-tracing calculation while considering the total diffusivity above 80 km, and the total diffusivity profile is shown in Fig. 4b. Radiative and diffusive damping rates corresponding to event G1 observed over Gadanki are shown in Fig. 4c for illustration. It is seen that radiative damping rate is higher than the diffusive damping rate below 95 km. This is the case for the other 13 events (G2–G5 and H1–H9) as well.

5 Application of reverse ray tracing for the wave events

By using the background parameters and the ray-tracing equations, we trace back the ray path(s) to identify the GW source region(s). We used a Runge–Kutta fourth-order method for numerical integration at the time step of $\delta t = 100 \text{ m } C_{gz}^{-1}$, where 100 m is the height step downwards from 97 km (the peak altitude of the airglow layer) and C_{gz} is the vertical group velocity. As the ray-tracing treatment is valid only when WKB approximation holds well, the ray integration is terminated whenever the WKB approximation is violated. We terminated the ray (1) when m^2 became negative, which means that the wave cannot propagate vertically; (2) when intrinsic frequency was less than zero or approaching zero, which means that the wave reached a critical layer and is likely to break beyond this; (3) when the WKB parameter was approaching values greater than 1 (beyond which WKB approximation breaks); and (4) when square of vertical wave number was becoming greater than $1 \times 10^{-6} \text{ cyc}^2 \text{ m}^{-2}$ (approaching critical level) (Wrasse et al., 2006). We calculated the wave action and thus the amplitude along the ray path by including the damping. As the information on wave amplitudes cannot be unambiguously determined from the optical emission intensity measurements, we assumed the GW am-

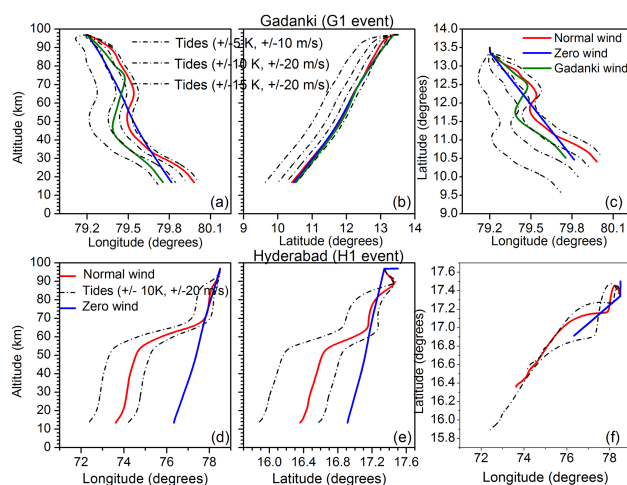


Figure 5. Ray paths for wave event G1 (starting at 97 km) in the (a) longitude–altitude, (b) latitude–altitude and (c) longitude–latitude cross sections. Ray paths obtained while considering different background wind conditions (normal wind, zero wind and Gadanki model wind) and the day-to-day variability of tides are also superimposed (dotted lines). Panels (d–f) are the same as (a–c) but for wave event H1. Note that the Gadanki atmospheric model wind is not used for the wave events over Hyderabad.

plitude as unity (at 97 km) and traced back the relative amplitudes along the ray path. Further, as we have not considered the local time variation of the background parameters, the ground-based wave frequency will be a constant. However, note that the intrinsic frequency still varies with altitude because of the varying background horizontal winds.

The observed and calculated GW parameters (intrinsic frequency; wave period; and zonal, meridional and vertical wave numbers) for all the wave events measured at the peak airglow emission altitudes as described in Sect. 2.1 and 2.2 are given as initial parameters to the ray-tracing code. We considered all the different combinations of observed wave parameters including the errors in the observations for obtaining the ray paths and the uncertainties in them. Note that atmospheric tides have large amplitudes in the MLT region which, at times, can be comparable to those of the background wind. As mentioned earlier, though tidal amplitudes are considered in the HWM-07 model, their day-to-day variability is not taken into account in the model. Amplitudes of the tides may reach values as high as 20 m s^{-1} over equatorial latitudes (Tsuda et al., 1999). As already mentioned, we have included day-to-day variability of tidal amplitudes into temperature and winds. In general, above the stratopause, tidal amplitudes are large and increase exponentially with altitude. It is interesting to note that (figure not shown) the variability in the background atmospheric parameters developed using data from a suite of instruments as mentioned above lies within the variability due to tides. Ray path calculations are also carried out for these background profiles.

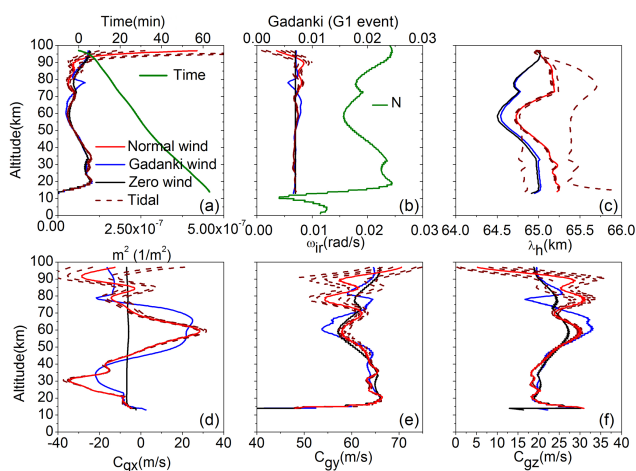


Figure 6. Profiles of (a) the square of vertical wave number (m^2), (b) intrinsic frequency (ω_{ir}) and Brunt–Väisälä frequency (N) (green); (c) horizontal wavelength; and (d) zonal, (e) meridional and (f) vertical group velocities for wave event G1. Profiles of the same obtained while considering the three different background winds (different colored lines) and the day-to-day variability of tides are also superimposed (dotted lines) in the respective panels. The observation time at the ray start and corresponding times along the ray time is also shown in (a) with the axis on the top.

We traced the ray path using the above initial parameters from the initial latitude ($13.5^\circ\text{N}/17.5^\circ\text{N}$), longitude ($79.2^\circ\text{E}/78.5^\circ\text{E}$) and altitude (97 km). The ray paths for wave event G1 with the longitude–altitude, latitude–altitude and longitude–latitude are shown in Fig. 5a–c, respectively, for Gadanki and in Fig. 5d–f for (H1) Hyderabad. Ray paths obtained while considering different background conditions (normal wind, zero wind and Gadanki model wind) and the day-to-day variability of tides are also superimposed with dotted lines. When we considered zero (Gadanki) wind, a shift of 71 km (25 km) in the horizontal position of the terminal point is observed with respect to that for normal wind for wave event G1. The shift reduced to 19 km and increased to 47 and 97 km when we considered the tidal variability of $+5\text{ K}$, $+10\text{ m s}^{-1}$; $+10\text{ K}$, $+20\text{ m s}^{-1}$; and $+15\text{ K}$, $+30\text{ m s}^{-1}$, respectively, with respect to the normal wind. The shift is $\sim 15\text{ km}$ for the tidal variability of -5 K , -10 m s^{-1} . The ray terminated in the mesosphere itself for tidal variability of -10 K , -20 m s^{-1} and -15 K , -30 m s^{-1} (figure not shown).

Over Hyderabad, for wave event H1, shown in Fig. 5d–f, the shifts in the horizontal location of the terminal point are 305.6 km (148.7 km) for tidal variability of $+10$, $+20\text{ m s}^{-1}$ (-10 K , -20 m s^{-1}) with reference to zero wind. This difference is only 59.5 km for tidal variability of -10 K , -20 m s^{-1} with respect to the normal wind. The terminal point locations for the rest of the wave events for normal winds are listed in Table 1. Note that, out of the five wave events over Gadanki, two wave events (G3 and G4) were

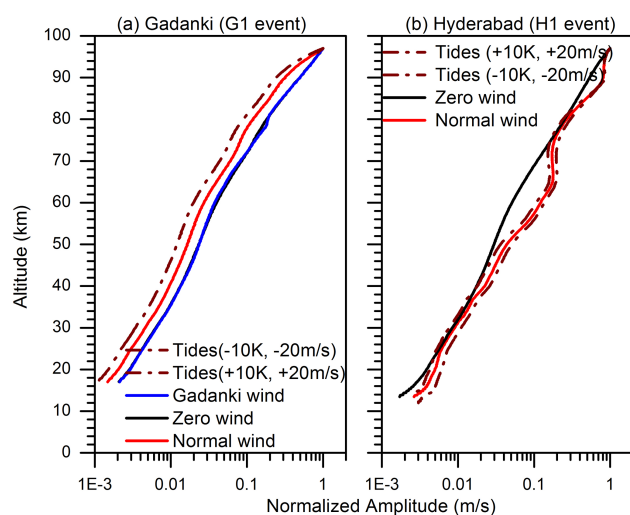


Figure 7. Normalized amplitudes of gravity waves observed for wave events (a) G1, and (b) H1, over Gadanki and Hyderabad, respectively. Amplitudes with three different background wind conditions along with different tidal amplitudes are also shown.

terminated in the upper mesosphere itself and one (G5) was terminated at 67 km. Over Hyderabad, out of the nine wave events, two wave events (H4 and H7) were terminated at $\sim 67\text{ km}$. In general, all the wave events which propagated down to the upper troposphere terminated between 10 and 14.5 km, except for case G2, which was terminated at 17 km due to violation of the WKB approximation. The violation of the WKB approximation at 17 km could be due to sharp temperature gradients near tropopause.

Profiles of the square of vertical wave number (m^2); intrinsic frequency (ω_{ir}) and Brunt–Väisälä frequency (N); horizontal wavelength (λ_h); and zonal, meridional and vertical group speed for the event G1 are shown in Fig. 6a–f, respectively. Profiles of these parameters obtained for different background wind conditions (normal wind, zero wind and Gadanki model wind) and the day-to-day variability of tides are also superimposed in the respective panels. The differences with and without the variability of tides in the parameters mentioned above are small below the stratopause and quite high above. Note that the effect of Doppler shifting of the wave frequency is larger at higher altitudes due to higher wind amplitudes. Around 13 km, the Brunt–Väisälä frequency is less than that of the intrinsic frequency, and thus the square of the vertical wave number is negative there (Fig. 6b). The variation in the horizontal wavelength with height (Fig. 6c) is small. Zonal group speed shows (Fig. 6d) nearly the same behavior as that of the zonal wind. The intrinsic frequency, ω_{ir} , exceeded N at 13 km altitude, and due to this m^2 became negative and the ray path was terminated there. The observation time at the ray start and the times along the ray time shown in Fig. 6a reveal that it took 63 min for the ray propagation.

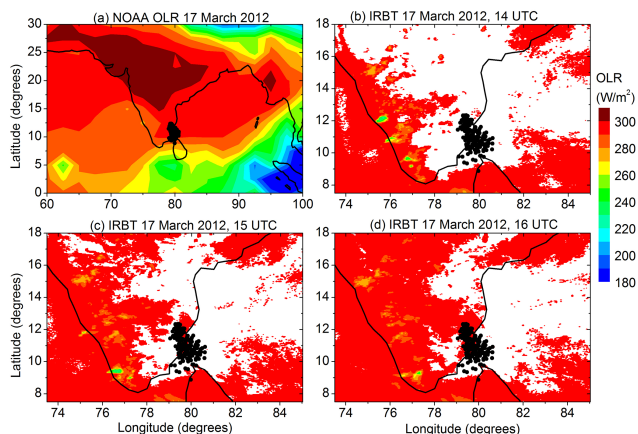


Figure 8. Daily mean latitude–longitude section of (a) OLR observed using NOAA products over the Indian region on 17 March 2012. Panels (b–d) are the same as (a) but for IR BT observed at 14:00, 15:00 and 20:00 UTC, respectively. Open (closed) circles in (a) (b–d) depict the terminal points of the ray paths shown in Fig. 4.

As mentioned earlier, the information on the wave amplitudes is not available from the observations. Therefore we used the GW amplitude as unity (at the altitude of observation) and traced back the relative amplitudes along the ray path. Profiles of amplitudes of GWs observed for wave events G1 and H1 over Gadanki and Hyderabad are shown in Fig. 7a and b, respectively. Amplitudes with three different background wind conditions along with different tidal amplitudes are also shown in the respective panels. Unity wave amplitude at the observed region translates to an amplitude of 10^{-3} near the source region. Amplitude growth is found to be higher when either Gadanki or zero wind models are considered and slightly lower for the normal wind. The growth is highly reduced when tidal variability in the background wind is considered. However, higher-amplitude growth rates were obtained over Hyderabad when we considered normal wind along with tidal variability as opposed to zero wind. Similar growth rates are also obtained for other wave events (not shown). Thus, background winds play an important role in the growth rates of GWs.

6 Discussion on the potential source(s) of the GW events

The geographical locations of the terminal points for different combinations of background winds along with different combinations of tidal variability are shown in Figs. 8 and 9 for the Gadanki and Hyderabad wave events, respectively. In these figures, the contour encircling all the points (not drawn in the panels of the figure) represents the horizontal spread of uncertainty due to background conditions (including tidal variability). The terminal point of the ray (in the troposphere) is expected to be the location of the GW source. Since 9 out

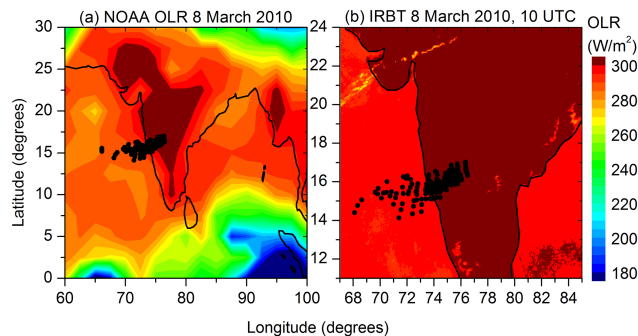


Figure 9. Same as Fig. 8 but for wave events observed over Hyderabad on 8 March 2010. Note that IR BT is shown only for 10:00 UTC.

of 14 wave events were terminated between 10 and 17 km, we search for the possible sources around this altitude at the location.

In general, primary sources for the GW generation over tropics are orography, convection and vertical shear in the horizontal winds. In the present case, GWs are unlikely to be the orographic origin as the observed waves have phase speeds much greater than zero. Tropical deep convection is assumed to be a primary source of the generation of a wide spectrum of GWs in the tropical latitudes. As mentioned earlier, OLR/IR BT is considered to be the proxy for the tropical deep convection. The lower the OLR/BT values, the higher the cloud top and hence the deeper the convection. OLR (IR BT) $< 240 \text{ W m}^{-2}$ (K) is taken to represent deep convection. However, convection may exist at locations away from the observational site, and waves generated at those locations can propagate to the mesospheric altitudes over the site. In order to see the presence or otherwise of convection in the vicinity of the termination location, a latitude–longitude cross section of NOAA-interpolated OLR obtained for 17 March 2012 (8 March 2010) is shown in Fig. 8a (Fig. 9a) for the Gadanki (Hyderabad) region. The terminal points of the rays for wave events G1 and G2 (H1–H9 except H4 and H7) with different background wind conditions and different combinations of variability of the tides are also shown in the figure. There is no convection in and around the Gadanki (Hyderabad) region, as can be noticed from this figure. Note that this plot is with a coarse grid ($2.5^\circ \times 2.5^\circ$ latitude–longitude) averaged for a day. The observed GWs could be generated due to localized sources having shorter temporal and spatial scales than those seen from the NOAA OLR data used. In order to examine this, we have used IR BT data which are available at $4 \text{ km} \times 4 \text{ km}$ grid size and on a half-hour basis. Latitude and longitude section of hourly IR BT at 14:00 (10:00), 15:00 and 16:00 UTC is shown in Fig. 8b–d (Fig. 9b), respectively. The terminal points with and without variability of the tides are also shown. Interestingly no cloud patches are seen at any of the times mentioned above. Thus, convection can be ruled out as a possible source of the observed wave events.

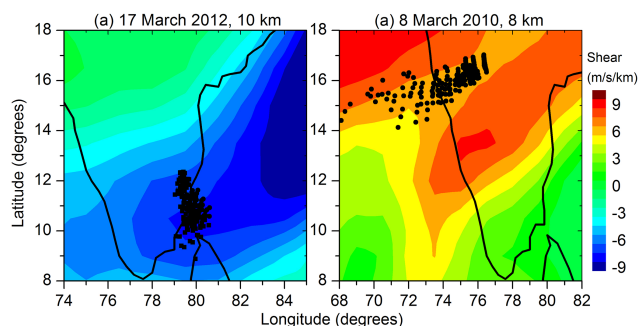


Figure 10. Latitude–longitude section of vertical shear in the horizontal wind observed using ERA-Interim data products on (a) 17 March 2012 at 10 km and (b) 8 March 2010 at 8 km. Filled circles show the terminal points of the ray paths estimated using three different wind conditions and tidal amplitudes.

The other possible source of GW generation is the vertical shear of the horizontal wind. The vertical shear in horizontal winds at an altitude of 10 km (8 km) on 17 March 2012 (8 March 2010) as a function of latitude–longitude is shown in Fig. 10a (Fig. 10b). The terminal points of the rays for both the wave events with and without the day-to-day variability of the tides are also shown in the figure. Interestingly, at all the terminal points (in the troposphere), strong vertical shear in the horizontal wind is seen, which is quite high ($8\text{--}9\text{ m s}^{-1}\text{ km}^{-1}$). In order to see whether these waves could be generated due to nonlinear interaction (through Kelvin–Helmholtz instability, KHI), the Richardson number ($Ri = \frac{N^2}{(dU/dz)^2}$) for the nearest location is calculated (using nearby radiosonde data) and is shown in Fig. 11. From the figure it can be noticed that $Ri < 0.25$, showing that Ri satisfies the condition for instability for the observed waves at both the stations. Thus, the shear is unstable and hence conducive for the excitation of KHI, leading to the generation of the propagating GWs through nonlinear interaction. Note that shear excitation of the GWs has been examined theoretically using both linear and nonlinear approaches (e.g., Fritts, 1982, 1984; McIntyre, 1978). For the excitation of radiating GWs by KHIs at a shear layer, the two mechanisms that are examined are the vortex pairing (sub-harmonic interaction) and envelope radiation (Fritts, 1984). The vortex pairing is found to be highly dependent on the minimum Ri , whereas the envelope radiation mechanism is found to provide efficient radiating wave excitation in the absence of propagating unstable modes (Fritts, 1984). Theoretical and numerical simulation work needs to be carried out to examine which of these mechanisms is adequate for the observed events in the present study. This aspect is beyond the scope of the present study and is planned to be taken up in the future.

Note that five wave events terminated at mesospheric altitudes. We examined the background atmospheric condition which can lead to the termination of these wave events at such high altitudes. The ray paths for two wave events ob-

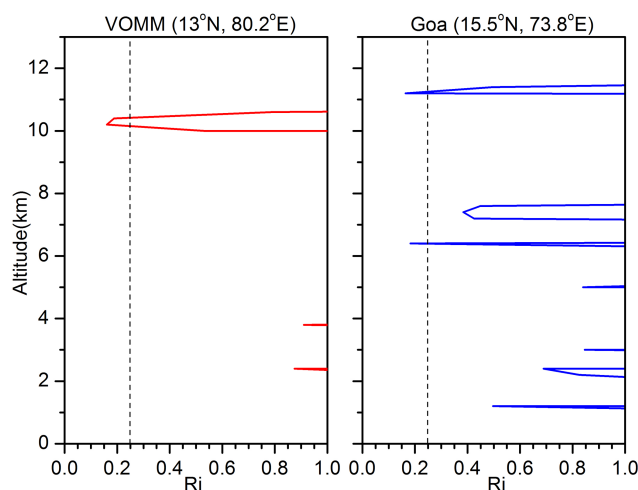


Figure 11. Profiles of Richardson number calculated close to the termination point using radiosonde data for the (a) Gadanki and (b) Hyderabad locations.

served on the same day over Gadanki could propagate down below with the same background atmosphere. When wave parameters related to this event are examined (Table 1), it can be seen that the phase speeds are small when compared to the other two wave events. We have introduced a wave at around 15 km, with all the wave parameters similar to that observed at 97 km for this event, and applied forward ray tracing. It is seen that the ray propagated up to 50 km and was terminated. Note that strong vertical shear in the background wind is seen at this altitude (Fig. 3). To investigate the role of shear in the process of propagation of waves, the shear is reduced to almost 0 in the 50–80 km altitude region. Under such conditions this wave event also could propagate to ~ 16 km in the reverse ray tracing. This reveals that the background wind shear is obstructing the ray path. It is quite likely that the wave was ducted between 50 and 80 km, and similar results are obtained for the other cases which were terminated in the mesosphere. This indicates that wind shears at mesospheric altitudes are responsible for termination at mesospheric altitudes for these events.

7 Summary and conclusions

Identification of the GW sources for the 14 wave events observed over Gadanki and Hyderabad using optical airglow measurements is presented. A reverse ray-tracing method is developed to obtain the location of the source regions of the GWs in the troposphere/mesosphere. We made use of the MSISE-90 model for temperature and the HWM-07 model for the zonal and meridional winds in addition to the ERA-Interim products in the lower atmosphere (1000 to 1 hPa pressure levels) and the Gadanki climatological model and zero wind model for the background atmosphere. We have

also incorporated the expected variability of tidal amplitudes of 5, 10 and 15 K in temperature and 10, 20 and 30 m s^{-1} in wind, respectively. The terminal points lie in the range of 50–100 and 60–300 km for Gadanki and Hyderabad, respectively, when different wind and tidal variabilities are used. Wave action is implemented taking into account the radiative and diffusive damping. Considering the wave amplitude as unity at 97 km, the amplitude of the wave is traced back to the source region for different wind models. Out of the 14 events examined, 9 ray paths terminated in the troposphere. The remaining 5 events were terminated in the mesosphere itself. We examined for possible sources for the 9 events where the ray paths terminated in the troposphere.

Orography as the possible source was ruled out, as wave events have high phase speeds. No tropical deep convection in and around Gadanki and Hyderabad was noticed near the ray terminal points. Interestingly, strong vertical shear in the horizontal wind is observed near the terminal points, and these large shears are considered to be the source of the GW events observed at the mesospheric altitudes. Preusse et al. (2008) discussed the transparency of the waves to the atmosphere in different seasons. They reported that, during equinox times, the atmosphere is more transparent to the high phase speed and shorter horizontal wavelength waves than it is in the solstices. Waves with shorter (< 10 km) horizontal wavelengths tend to be removed by vertical reflection or evanescence at the source, and slower phase speeds are more prone to the critical-level removal. This leads to a preference for waves with longer horizontal wavelengths and faster ground-based phase speeds to reach the MLT. However, they observed that many rays penetrated into the MLT at the tropical latitude where wind speed is low in comparison to the mid- and high latitudes. In our case, whenever phase speed was low for short horizontal wavelength waves, the wave did not reach the troposphere and was stopped at mesospheric altitude itself. While there is strong evidence for convectively generated gravity waves, evidence of tropospheric wind-shear-generated GWs is rather sparse (Mastrantonio 1976; Fritts and Alexander 2003). The present study clearly demonstrated that high-frequency, high-phase-speed GWs observed in the mesosphere can be generated by tropospheric wind shear. Examination of the background wind conditions and wave parameters for the events that were terminated in the mesosphere revealed that the phase speeds were quite small for these strong vertical shears in the 50–80 km region (and at 95 km), resulting in termination of the ray paths. A potential explanation is that the waves generated in the troposphere are ducted between 50 and 80 km and the waves observed above this region are due to leakage of waves from the duct. It is also likely that the observed GWs in these cases (G3, G4, G5, H5 and H7) are from secondary wave generation due to wave breaking at the termination region. While secondary wave generation due to convectively generated waves has been investigated (e.g., Zhou et al., 2002; Chun and Kim, 2008), such investigations have not yet been

carried out for GWs of shear origin. This aspect needs further investigation. Note that we have tested the reverse ray-tracing method successfully for 14 wave events. Further, wave action is also implemented successfully by assuming the wave amplitudes as unity, as information on the same is not available from optical observations. However, a greater number of cases need to be examined, particularly for the events that occur during the Indian summer monsoon season, when convection and strong vertical shears in the horizontal winds co-exist due to the prevailing Tropical Easterly Jet (Venkat Ratnam et al., 2008). A few experiments are planned to be conducted at Gadanki with simultaneous operation of MST radar, radiosondes, Rayleigh lidar, airglow imagers and meteor radar that can together provide information right from the troposphere to the MLT region. Note that such a study on the vertical propagation of mesoscale gravity wave from the lower to upper atmosphere was performed recently by Shin Suzuki et al. (2013) using an airglow imager and lidar over the Arctic region.

Acknowledgements. This work was done as a part of the SAFAR and CAWSES India phase II programs. We thank the NARL staff for providing data used in the present study. We are deeply grateful to NOAA and ECMWF for providing OLR and ERA-Interim data, respectively, used in the present study through their ftp sites. HWM-07 model data are obtained from <http://nssdcftp.gsfc.nasa.gov/models/atmospheric/hwm07/>. This work is supported by the Department of Space, Government of India.

Edited by: W. Ward

References

- Alexander, M. J., Holton, J. R., and Durran, D. R.: The gravity wave response above deep convection in a squall line simulation, *J. Atmos. Sci.*, 52, 2212–2226, 1995.
- Alexander, M. J., Geller, M., McLandress, C., Polavarapu, S., Preusse, P., Sassi, F., Sato, K., Eckermann, S., Ern, M., Hertzog, A., Kawatani, Y., Pulido, M., Shaw, T. A., Sigmund, M., Vincent, R., and Watanabe, S.: Recent developments in gravity-wave effects in climate models, and the global distribution of gravity-wave momentum flux from observations and models, *Q. J. R. Meteorol. Soc.*, 136, 1103–1124, 2010.
- Brown, L. B., Gerrard, A. J., Meriwether, J. W., and Makela, J. J.: All-sky imaging observations of mesospheric fronts in OI 557.7 nm and broadband OH airglow emissions: Analysis of frontal structure, atmospheric background conditions, and potential sourcing mechanisms, *J. Geophys. Res.*, 109, D19104, doi:10.1029/2003JD004223, 2004.
- Chun, H. Y. and Kim, Y. H.: Secondary waves generated by breaking of convective gravity waves in the mesosphere and their influence in the wave momentum flux, *J. Geophys. Res.*, 113, D23107, doi:10.1029/2008JD009792, 2008.

- Clark, T. L., Hauf, T., and Kuettner, J. P.: Convectively forced internal gravity waves: Results from two-dimensional numerical experiments, *Q. J. R. Meteorol. Soc.*, 112, 899–925, doi:10.1002/qj.49711247402, 1986.
- Debashis Nath., Venkat Ratnam, M., Jagannadha Rao, V. V. M., Krishna Murthy, B. V., and Vijaya Bhaskara Rao, S.: Gravity wave characteristics observed over a tropical station using high-resolution GPS radiosonde soundings, *J. Geophys. Res.*, 114, D06117, doi:10.1029/2008JD011056, 2009
- Dee, D. P., Uppala, S. M., Simmons, A. J., Berrisford, P., Poli, P., Kobayashi, S., Andrae, U., Balmaseda, M. A., Balsamo, G., Bauer, P., Bechtold, P., Beljaars, A. C. M., van de Berg, L., Bidlot, J., Bormann, N., Delsol, C., Dragani, R., Fuentes, M., Geer, A. J., Haimberger, L., Healy, S. B., Hersbach, H., Hólm, E. V., Isaksen, I., Kållberg, P., Köhler, M., Matricardi, M., McNally, A. P., Monge-Sanz, B. M., Morcrette, J.-J., Park, B. K., Peubey, C., de Rosnay, P., Tavolato, C., Thépaut, J.-N., and Vitart, F.: The ERA-Interim-reanalysis: configuration and performance of the data assimilation system, *Q. J. R. Meteorol. Soc.*, 137, 553–597, 2011.
- Dhaka, S. K., Choudhary, R. K., Malik, S., Shibagaki, Y., Yamanaka, M. D., and Fukao, S.: Observable signatures of a convectively generated wave field over the tropics using Indian MST radar at Gadanki (13.5° N, 79.2° E), *Geophys. Res. Lett.*, 29, 1872, doi:10.1029/2002GL014745, 2002.
- Drob, D. P., Emmert, J. T., Crowley, G., Picone, J. M., Shepherd, G. G., Skinner, W., Hays, P., Niciejewski, R. J., Larsen, M., She, C. Y., Meriwether, J. W., Hernandez, G., Jarvis, M. J., Sipler, D. P., Tepley, C. A., O'Brien, M. S., Bowman, J. R., Wu, Q., Murayama, Y., Kawamura, S., Reid, I. M., and Vincent, R. A.: An empirical model of the Earth's horizontal wind fields: HWM07, *J. Geophys. Res.*, 113, A12304, doi:10.1029/2008JA013668, 2008.
- Dutta, G., Ajay Kumar, M. C., Vinay Kumar, P., Venkat Ratnam, M., Chandrashekar, M., Shibagaki, Y., Salauddin, M., and Basha, H. A.: Characteristics of high-frequency gravity waves generated by tropical deep convection: Case studies, *J. Geophys. Res.*, 114, D18109, doi:10.1029/2008JD011332, 2009.
- Eckermann, S. D.: Ray-tracing simulation of the global propagation of inertia gravity waves through the zonally averaged middle atmosphere, *J. Geophys. Res.*, 97, 15849–15866, 1992.
- Fovell, R., Durran, D., and Holton, J. R.: Numerical simulations of convectively generated stratospheric gravity waves, *J. Atmos. Sci.*, 49, 1427–1442, 1992.
- Fritts, D. C.: Shear Excitation of Atmospheric Gravity Waves, *J. Atmos. Sci.*, 39, 1936–1952, 1982.
- Fritts, D. C.: Shear Excitation of Atmospheric Gravity Waves, Part II: Nonlinear Radiation from a Free Shear Layer, *J. Atmos. Sci.*, 41, 524–537, 1984.
- Fritts, D. C. and Alexander, M. J.: Gravity wave dynamics and effects in the middle atmosphere, *Rev. Geophys.*, 41, doi:10.1029/2001RG000106, 2003.
- Fritts, D. C., Sharon, L., Vadas, K. W., and Werne, J. A.: Mean and variable forcing of the middle atmosphere by gravity waves, *J. Atmos. Sol. Terr. Phys.*, 68, 247–265, 2006.
- Geller, M. A., Alexander, M. J., Love, P. T., Bacmeister, J., Ern, M., Hertzog, A., Manzini, E., Preusse, P., Sato, K., Scaife, A., and Zhou, T.: A comparison between gravity wave momentum fluxes in observations and climate models, *J. Climate*, 26, 6383–6405, doi:10.1175/JCLI-D-12-00545.1, 2013.
- Gerrard, A. J., Kane, T. J., Eckermann, S. D., and Thayer, J. P.: Gravity waves and mesospheric clouds in the summer middle atmosphere: A comparison of lidar measurements and ray modeling of gravity waves over Sondrestrom, Greenland, *J. Geophys. Res.*, 109, D10103, doi:10.1029/2002JD002783, 2004.
- Guest, F. M., Reeder, M. J., Marks, C. J., and Karoly, D. J.: Inertia-Gravity Waves Observed in the Lower Stratosphere over Macquarie Island, *J. Atmos. Sci.*, 57, 2000.
- Hecht, J. H., Walterscheid, R. L., and Ross, M. N.: First measurements of the two-dimensional horizontal wave number spectrum from CCD images of the nightglow, *J. Geophys. Res.*, 99, 11449–11460, 1994.
- Hedin, A. E.: Extension of the MSIS Thermosphere model into the middle and Lower atmosphere, *J. Geophys. Res.*, 96, 1159–117, 1991.
- Hertzog, A., Souprayen, C., and Hauchecorne, A.: Observation and backward trajectory of an inertio-gravity wave in the lower stratosphere, *Ann. Geophys.*, 19, 1141–1155, 2001, <http://www.ann-geophys.net/19/1141/2001/>.
- Hocking, W. K.: The effects of middle atmosphere turbulence on coupling between atmospheric regions, *J. Geomag., Geoelec.*, 43, 621–636, 1991.
- Janowiak, J. E., Joyce, R. J., and Yarosh, Y.: A real-time global half-hourly pixel-resolution IR dataset and its applications, *Bull. Amer. Meteor. Soc.*, 82, 205–217, 2001.
- Jones, W. L.: Ray tracing for internal gravity waves, *J. Geophys. Res.*, 74, 2028–2033, 1969.
- Kumar, K. K.: VHF radar observations of convectively generated gravity waves: Some new insights, *Geophys. Res. Lett.*, 33, L01815, doi:10.1029/2005GL024109, 2006.
- Kumar, K. K.: VHF radar investigations on the role of mechanical oscillator effect in existing convectively generated gravity waves, *Geophys. Res. Lett.*, 34, L01803, doi:10.1029/2006GL027404, 2007.
- Kishore Kumar, G., Venkat Ratnam, M., Patra, A. K., Vijaya Bhaskara Rao, S., and Russell, J.: Mean thermal structure of the low-latitude middle atmosphere studied using Gadanki Rayleigh lidar, Rocket, and SABER/TIMED observations, *J. Geophys. Res.*, 113, D23106, doi:10.1029/2008JD010511, 2008a.
- Kishore Kumar, G., Venkat Ratnam, M., Patra, A. K., Jagannadha Rao, V. V. M., Vijaya Bhaskara Rao, S., Kishore Kumar, K., Gurubaran, S., Ramkumar, G., and Narayana Rao, D.: Low-latitude mesospheric mean winds observed by Gadanki mesosphere-stratosphere-troposphere (MST) radar and comparison with Rocket, High Resolution Doppler Imager (HRDI), and MF radar measurements and HWM93, *J. Geophys. Res.*, 113, D19117, doi:10.1029/2008JD009862, 2008b.
- Laskar, F. I., Pallamraju, D., Vijaya Lakshmi, T., Anji Reddy, M., Pathan, B. M., and Chakrabarti, S.: Investigations on vertical coupling of atmospheric regions using combined multiwavelength optical dayglow, magnetic, and radio measurements, *J. Geophys. Res. Space Physics.*, 118, 4618–4627, doi:10.1002/jgra.50426, 2013.
- Leena, P. P., Venkat Ratnam, M., KrishnaMurthy, B. V., and VijayaBhaskaraRao, S.: Detection of high frequency gravity waves using high resolution radiosonde observations, *J. Atmos. Sol. Terr. Phys.*, 77, 254–259, 2012a.

- Leena, P. P., Venkat Ratnam, M., and Krishna Murthy, B. V.: Inertia gravity wave characteristics and associated fluxes observed using five years of radiosonde measurements over a tropical station, *J. Atmos. Sol. Terr. Phys.*, 84–85, 37–44, 2012b.
- Lilly, D. K. and Kennedy, P. J.: Observations of a stationary mountain wave and its associated momentum flux and energy dissipation, *J. Atmos. Sci.*, 30, 1135–1152, 1973.
- Mastrantonio, G., Einaudi, F., Fua, D., and Lalas, D. P.: Generation of gravity waves by jet streams in the atmosphere, *J. Atmos. Sci.*, 33, 1730–1738, 1976.
- Marks, C. J. and Eckermann, S. D.: A three-dimensional non-hydrostatic ray-tracing model for gravity waves: formulation and preliminary results for the middle atmosphere, *J. Atmos. Sci.*, 52, 1959–1984, 1995.
- McIntyre, M. E. and Weissman, M. A.: On Radiating Instabilities and resonant over-reflection, *J. Atmos. Sci.*, 35, 1190–1196, 1978.
- Nakamura, T., Aono, T., Tsuda, T., Admiranto, A. G., and Achmad Suranto, E.: Mesospheric gravity waves over a tropical convective region observed by OH airglow imaging in Indonesia, *Geophys. Res. Lett.*, 30, 1882–1885, 2003.
- Narayana Rao, D., Ratnam, M. V., Rao, T. N., and Rao, S. V. B.: Seasonal variation of vertical eddy diffusivity in the troposphere, lower stratosphere and mesosphere over a tropical station, *Ann. Geophys.*, 19, 975–984, 2001, <http://www.ann-geophys.net/19/975/2001/>.
- Nastrom, G. D. and Fritts, D. C.: Sources of mesoscale variability of gravity waves I: topographic excitation, *J. Atmos. Sci.*, 49, 101–110, 1992.
- O’Sullivan, D. and Dunkerton, T. J.: Generation of Inertia Gravity waves in a simulated life cycle of Baroclinic Instability, *J. Atmos. Sci.*, 52, 1995.
- Pallamraju, D., Laskar, F. I., Singh, R. P., Baumgardner, J., and Chakrabarti, S.: MISE: A Multiwavelength Imaging Spectrograph using Echelle grating for daytime optical agronomy investigations, *J. Atmos. Sol-Terr. Phys.*, 103, 176–183, 2013.
- Pallamraju, D., Baumgardner, J., Singh, R. P., Laskar, F. I., Mendillo, C., Cook, T., Lockwood, S., Narayanan, R., Pant, T. K., and Chakrabarti, S.: Daytime wave characteristics in the mesosphere lower thermosphere region: results from the balloon-borne investigations of regional-atmospheric dynamics experiment, *J. Geophys. Res.*, 119, 2229–2242, doi:10.1002/2013JA019368, 2014.
- Pfister, L., Chan, K. R., Bui, T.P., Bowen, S., Legg, M., Gary, B., Kelly, K., Proffitt, M. and Starr, W.: Gravity Waves Generated by a Tropical Cyclone During the STEP Tropical Field Program: A Case Study, *J. Geophys. Res.*, 98, D5, 1993.
- Piani, C., Durran, D., Alexander, M. J., and Holton, J. R.: A numerical study of three-dimensional gravity waves triggered by deep tropical convection and their role in the dynamics of the QBO, *J. Atmos. Sci.*, 57, 3689–3702, doi:10.1175/1520-0469(2000)057<3689, 2000.
- Plougonven, R. and Zhang, F.: Internal gravity waves from atmospheric jets and fronts, *Rev. Geophys.*, 52, 33–76, doi:10.1002/2012RG000419, 2014.
- Preusse, P., Eckermann, S. D., and Ern, M.: Transparency of the atmosphere to short horizontal wavelength gravity waves, *J. Geophys. Res.*, 113, D24104, doi:10.1029/2007JD009682, 2008.
- Queney, P.: The problem of air flow over mountains: A summary of theoretical results, *Bull. Am. Meteorol. Soc.*, 29, 16–26, 1948.
- Salby, M. L. and Garcia, R. R.: Transient response to localized episodic heating in the Tropics, Part 1: Excitation and short-time Near field behavior, *J. Atmos. Sci.*, 44, 458–498, 1987.
- Schoeberl, M. R.: A ray tracing model of gravity wave propagation and breakdown in the middle atmosphere, *J. Geophys. Res.*, 90, 7999–8010, doi:10.1029/JD090iD05p07999, 1985.
- Suzuki, S., Lubkena, F.-J., Baumgarten, G., Kaifler, N., Eixmann, R., Williams, B. P., and Nakamura, T.: Vertical propagation of a mesoscale gravity wave from the lower to the upper atmosphere, *J. Atmos. Sol. Terr. Phys.*, 97, 29–36, 2013.
- Taori, A., Jayaraman, A., and Kamalakar, V.: Imaging of mesosphere–thermosphere airglow emissions over Gadanki (13.5° N, 79.2° E) – first results, *J. Atmos. Sol. Terr. Phys.*, 93, 21–28, 2013.
- Taylor, M. J., Pendleton, W. R. J., Clark, S., Takahashi, H., Gobbi, D., and Goldberg, R. A.: Image measurements of short-period gravity waves at equatorial latitudes, *J. Geophys. Res.*, 102, 26283–26299, 1997.
- Tsuda, T., Ohnishi, K., Isoda, F., Nakamura, T., Vincent, R. A., Reid, I. M., Harijono, S. W. B., Sribimawati, T., Nuryanto, A., and Wiryosumarto, H.: Coordinated radar observations of atmospheric diurnal tides in equatorial regions, *Earth Planets Space*, 51, 579–592, 1999.
- Vadas, S. L., Taylor, M. J., Pautet, P.-D., Stamus, P. A., Fritts, D. C., Liu, H.-L., São Sabbas, F. T., Rampinelli, V. T., Batista, P., and Takahashi, H.: Convection: the likely source of the medium-scale gravity waves observed in the OH airglow layer near Brasilia, Brazil, during the SpreadFEx campaign, *Ann. Geophys.*, 27, 231–259, doi:10.5194/angeo-27-231-2009, 2009.
- Venkat Ratnam, M., Narendra Babu, A., Jagannadha Rao, V. V. M., Vijaya Baskar Rao, S., and Narayana Rao, D.: MST radar and radiosonde observations of inertia-gravity wave climatology over tropical stations: source mechanisms, *J. Geophys. Res.*, 113, D07109, doi:10.1029/2007JD008986, 2008.
- Vincent, R. A. and Alexander, M. J.: Gravity waves in the tropical lower stratosphere: an observational study of seasonal and inter-annual variability, *J. Geophys. Res.*, 105, 17971–17982, 2000.
- Wrasse, C. M., Nakamura, T., Tsuda, T., Takahashi, H., Medeiros, A. F., Taylor, M. J., Gobbi, D., Salatun, A., Suratno, Achmad, E., and Admiranto, A. G.: Reverse ray tracing of the mesospheric gravity waves observed at 23° S (Brazil) and 7° S (Indonesia) in airglow imagers, *J. Atmos. Sol. Terr. Phys.*, 68, 163–181, 2006.
- Zhou, X. L., Holton, J. R., and Mullendore, G. L.: Forcing of secondary waves by breaking of gravity waves in the mesosphere, *J. Geophys. Res.*, 107, D7, 4058, doi:10.1029/2001JD001204, 2002.
- Zhu, X.: Radiative damping revisited: parameterization of damping rate in the middle atmosphere, *J. Atmos. Sci.*, 50, 3008–3012, 1993.